Cell Reports
Physical Science

CellPress
OPEN ACCESS

Article

# Atomically precise bimetallic metal ensembles with tailorable synergistic effects

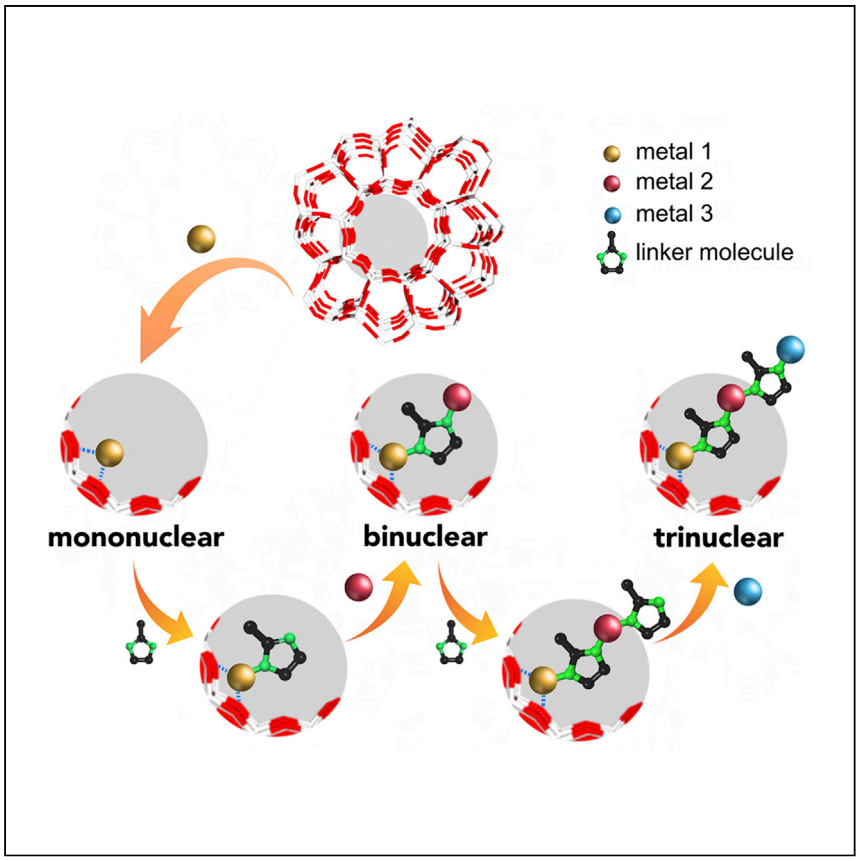


Chen et al. demonstrate the development of atom-precise supported metal ensembles, with controllable nuclearity and elemental composition, by a stepwise assembly method. The tunable electronic and steric properties of the active sites are achieved, bridging homogeneous and heterogeneous catalytic strategies.

Tianxiang Chen, Yong Wang, Qi Xue, ..., Shik Chi Edman Tsang, Kwok-yin Wong, Tsz Woon Benedict Lo

bolong.huang@polyu.edu.hk (B.H.)
kwok-yin.wong@polyu.edu.hk (K.-y.W.)
twblo@polyu.edu.hk (T.W.B.L.)

## Highlights

Synthesis of atom-precise supported metal ensembles

Controllable nuclearity and elemental composition by a stepwise assembly strategy

Synergistic effect by nearby metal nuclei for cooperative catalysis

Chen et al., Cell Reports Physical Science 3, 100850
April 20, 2022 
https://doi.org/10.1016/j.xcrp.2022.100850

Cell Reports
Physical Science

CellPress
OPEN ACCESS

Article

# Atomically precise bimetallic metal ensembles with tailorable synergistic effects

Tianxiang Chen,[1,2,9] Yong Wang,[1,2,9] Qi Xue,[1] Ching Kit Tommy Wun,[1] Pui Kin So,[1] Ka Fu Yung,[1] Tai-Sing Wu,[3] Yun-Liang Soo,[4] Keita Taniya,[5] Sarah Day,[6] Chiu C. Tang,[6] Zehao Li,[7] Bolong Huang,[1,2,*] Shik Chi Edman Tsang,[8] Kwok-yin Wong,[1,2,*] and Tsz Woon Benedict Lo[1,2,10,*]

## SUMMARY

**The large-scale synthesis of supported multinuclear catalysts with controllable metal nuclearity and constituent composition remains a formidable challenge. We report the stepwise assembly of supported atom-precise bimetallic ligand-mediated metal ensembles (LMMEs) by exploiting the underlying principles of coordination chemistry and solid-state chemistry. Lewis di-basic 2-methylimidazole is used to bridge multiple $Cu^{2+}$ and $M^{2+}$ (M = Co, Ni, Cu, and Zn) ions within ZSM-5 zeolites. We observe the metal constituent composition of the LMMEs by mass spectroscopy. The adjacent metal nuclei in the LMMEs offer substantial synergistic effects that enhance the catalytic performance by at least an order of magnitude in the model catalytic "click" reaction. It is envisaged that this stepwise assembly approach to develop supported multinuclear catalysts with atom precision could effectively bridge homogeneous and heterogeneous catalysis.**

## INTRODUCTION

Supported multinuclear catalysts are attracting considerable current attention in various applications as they are highly atom efficient and possess widely tunable electronic and geometric characteristics.[1–7] The development of this class of materials will bring heterogeneous catalysis toward the molecular frontier, where the molecular specificity of homogeneous catalysts can be preserved to the greatest extent.[8]

In contrast to mononuclear analogs, multinuclear catalysts could offer favorable reactivities due to the presence of adjacent metal nuclei (with or without direct metal-metal bonding). The metal nuclei in multinuclear catalysts may exhibit multiple oxidation states and different chemical characteristics.[9,10] Synergistic effects between nearby metal nuclei could yield transformation rates or selectivities not possible with mononuclear analogs.[11–14] The distance between the metal nuclei also influences the catalytic properties.[15] Although multinuclear complexes can be prepared by a conventional coordination-chemistry approach, including the preparation of various bimetallic complexes using double-decker ligands or specifically designed binucleating platforms,[16–19] the large-scale synthesis of atomically precise multinuclear species remains a formidable challenge. It is generally attributed to various intrinsic limitations, such as complicated ligand preparations and the separation of organometallic precursors, the direct formation issues of oligomers, and yielding products with uncontrolled metal ratios.[20–22]

To achieve this goal, we have creatively developed a stepwise assembly strategy to synthesize mono- and bimetallic ligand-mediated metal ensembles (LMMEs) by

[1]State Key Laboratory of Chemical Biology and Drug Discovery, Department of Applied Biology and Chemical Technology, The Hong Kong Polytechnic University, Hunghom, Hong Kong, China

[2]The Hong Kong Polytechnic University Shenzhen Research Institute, The Hong Kong Polytechnic University, Shenzhen 518057, China

[3]National Synchrotron Radiation Research Center, 101 Hsin-Ann Road, Hsinchu 30076, Taiwan

[4]Department of Physics, National Tsing Hua University, Hsinchu 30013, Taiwan

[5]Graduate School of Engineering / Department of Chemical Science and Engineering, Kobe University, Complex Fluid and Thermal Engineering Research Center (COFTEC), Kobe, Japan

[6]Diamond Light Source, Ltd., Harwell Science and Innovation Campus, Didcot, Oxfordshire, Harwell Campus, Oxford OX11 0DE, UK

[7]School of Chemistry and Chemical Engineering, Anyang Normal University, Anyang 455000, China

[8]Inorganic Chemistry Laboratory, Department of Chemistry, Oxford University, Oxford OX1 3QR, UK

[9]These authors contributed equally

[10]Lead contact

*Correspondence: bolong.huang@polyu.edu.hk (B.H.), kwok-yin.wong@polyu.edu.hk (K.-y.W.), twblo@polyu.edu.hk (T.W.B.L.)

https://doi.org/10.1016/j.xcrp.2022.100850

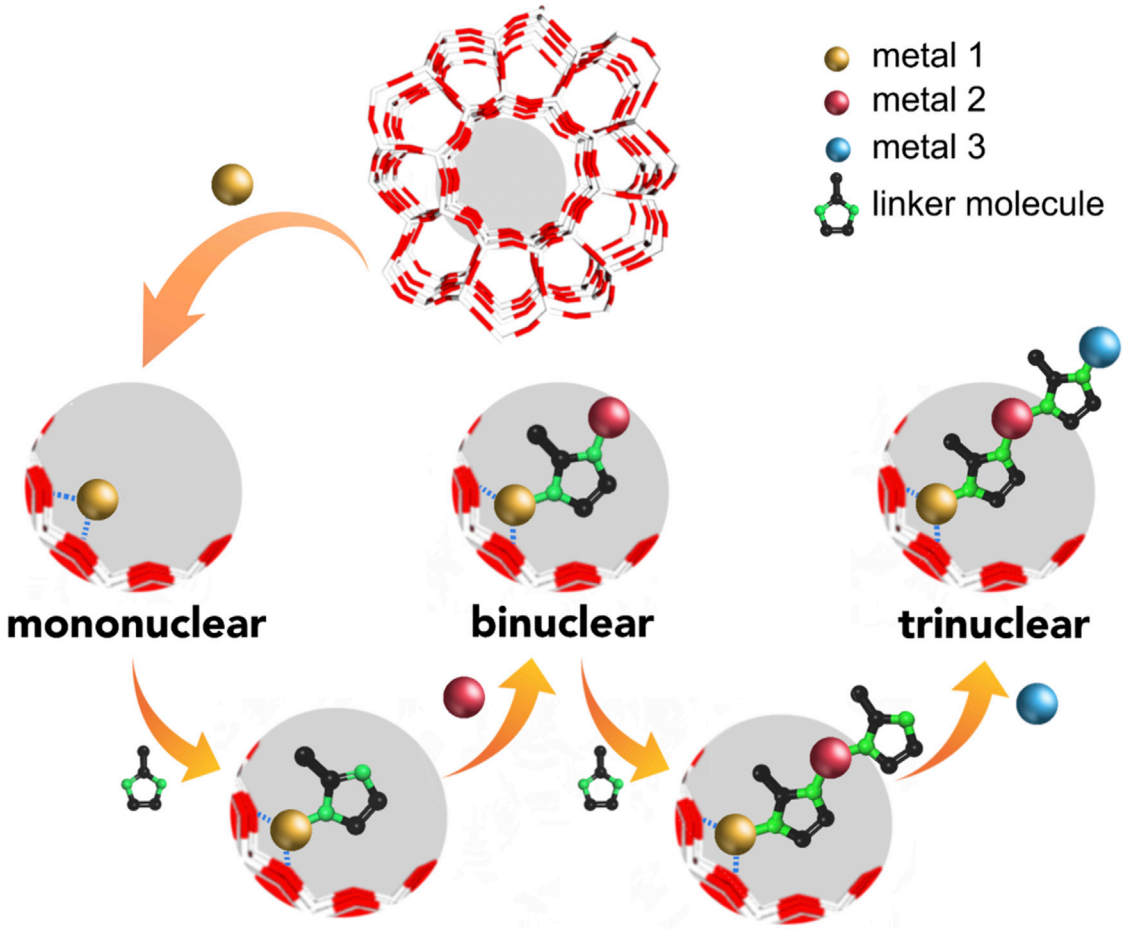


**Scheme 1. Schematic illustration showing the stepwise assembly strategy of Cu-based LMMEs in ZSM-5 zeolites**
Viewed along the crystallographic b axis, white and red sticks representing Al/Si and O, respectively. Coordinated water ligands are omitted for clarity.

harnessing the underlying principles of solid-state chemistry (via the confinement effect) and coordination chemistry (via the formation of acid-base adducts). We utilize the chemical and geometric specificity of 2-methylimidazole ("meIm") to assemble multiple mid-to-late *3d* transition metal ions in a stepwise manner, as meIm is di-basic in nature and possesses a rigid structure that can prevent it from chelating with the metal center. The synthesis of a series of Cu-based LMMEs, with controllable metal nuclearity and constituent composition, supported on zeolites can be achieved. Our LMMEs, excitingly, show tunable electronic and geometric properties that can regulate the catalytic landscape, as probed by our model Huisgen azide-alkyne cycloaddition "click" reaction.[23]

## RESULTS

### Stepwise assembly of LMMEs in ZSM-5 zeolites

The zeolitic Brønsted acid sites of H-ZSM-5 have been utilized to anchor $Cu^{2+}$ ions through conventional ion exchange. As illustrated in the stepwise assembly strategy in Scheme 1, we have further synthesized a series of meIm-mediated Cu-based LMMEs in ZSM-5 zeolites, including $Cu_x$-ZSM-5 ($x$ = 2 and 3) and Cu-*M*-ZSM-5, where M = Co, Ni, Zn (denoted $Cu_x$-Z and Cu-*M*-Z, respectively). The Cu content increases from 2.30 to 4.12 to 6.51 wt % for $Cu_1$-Z, $Cu_2$-Z, and $Cu_3$-Z, respectively (Table S1). It renders an atomic Cu:Al ratio of 1:1.9:2.7. In the control experiment without the

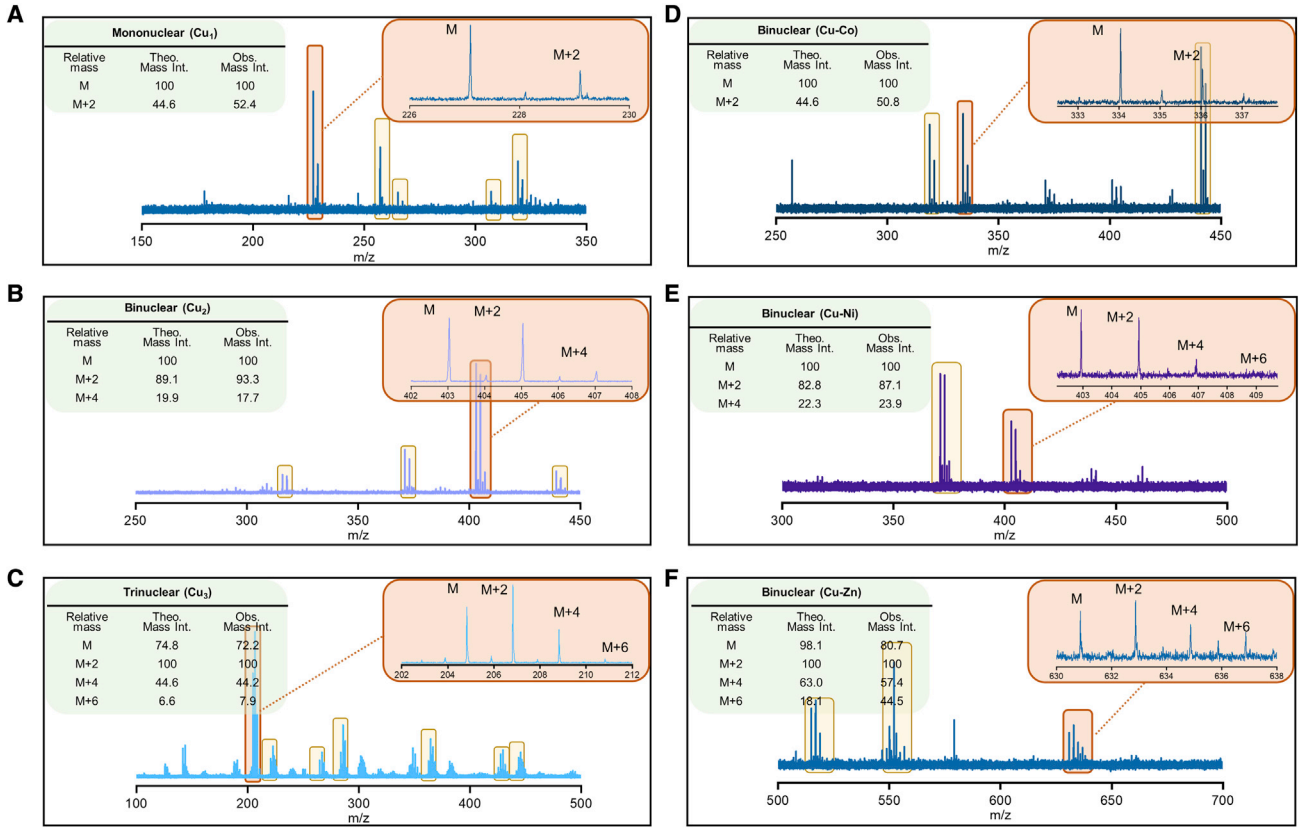


**Figure 1. Isotope-distribution analysis by mass spectroscopy**

(A–F) MALDI-TOF-TOF mass spectra of (A) $Cu_1$-meIm-Z, (B) $Cu_2$-Z, (C) $Cu_3$-Z, (D) Cu-Co-Z, (E) Cu-Ni-Z, and (F) Cu-Zn-Z. The theoretical mass intensity (theo. mass int.) analysis of the major features based on the relative isotope distribution of the proposed nuclear combinations is presented in the inset tables. The regions highlighted in brown are shown in the inset, whereas the regions highlighted in yellow show comparable mass-intensity distribution. We have not observed any multinuclear Cu-based features from $Cu_1$-meIm-Z, which indicates the absence of metal aggregation on the ionizing environment in the chamber.

See also Schemes S1 and S2.

addition of the meIm linker, the Cu content remains unchanged within experimental error. Similarly, the elemental ratios of Cu:Co, Cu:Ni, and Cu:Zn were determined as 1:0.59, 1:0.78, and 1:0.52, respectively. This comparative analysis is facile to evaluate the efficacy of the stepwise assembly strategy. See also supplemental experimental procedures.

To study the structural features of our samples, we used matrix-assisted laser desorption/ionization time-of-flight time-of-flight (MALDI-TOF-TOF) mass spectrometry. It has long been a highly reliable technique to direct the synthesis of related cluster complexes and the analysis of samples in solid states.[24] Hence, it is well suited for the evaluation of the LMMEs embedded in the insoluble zeolite hosts by systematic comparison with the theoretical mass intensity based on the isotope distribution of the substrates.[25,26] Figure 1 displays the MALDI-TOF-TOF mass spectra of $Cu_1$-Z modified with meIm ($Cu_1$-meIm-Z), $Cu_2$-Z, $Cu_3$-Z, Cu-Co-Z, Cu-Ni-Z, and Cu-Zn-Z. Remarkably different mass-intensity ratios are observed. Figure S1 shows the absence of structural features from $Cu_1$-Z, which suggests that the meIm ligand is necessary to facilitate the desorption of the embedded species from the zeolite host. In $Cu_1$-meIm-Z, the predominant peaks can be assigned to mononuclear Cu-based species (cf. the theoretical mass intensity M:(M+2) ratio of

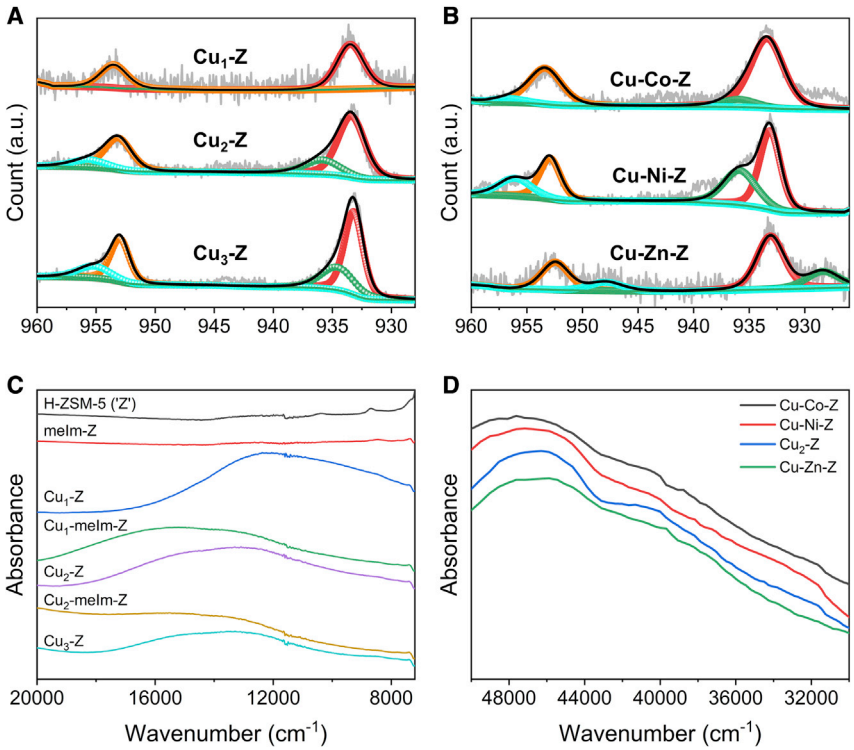


**Figure 2. Spectroscopic results showing the variations in electronic structures**

(A and B) Cu 2p X-ray photoelectron spectra of (A) $Cu_x$-Z and (B) Cu-*M*-Z.

(C and D) Selected regions of UV-vis-NIR diffuse reflectance spectra of (C) H-ZSM-5, $Cu_x$-Z, and $Cu_x$-meIm-Z and (D) Cu-*M*-Z. (See the full range of spectra in Figures S4 and S5).

single Cu is 100:44.6). A slight deviation from the theoretical value can be attributed to the presence of C, H, O, and N atoms. No significant feature of multinuclear Cu-based species is seen in the mass spectrum. The detailed derivations of the theoretical mass intensities are summarized in Schemes S1 and S2. In $Cu_2$-Z, the predominant feature can be assigned to binuclear $Cu_2$. We have also noted the occurrence of mononuclear Cu in the low mass range due to potential fragmentation and experimental residual of $Cu_1$. Similarly, the major mass-intensity ratios can be assigned to trinuclear $Cu_3$, with a minor occurrence of mononuclear Cu in the low mass region. Figures 1D–1F show the mass spectra of Cu-Co-Z, Cu-Ni-Z, and Cu-Zn-Z. Excitingly, their predominant features match excellently with the theoretical mass intensity ratios of binuclear Cu-Co, Cu-Ni, and Cu-Zn. The MALDI-TOF-TOF mass spectroscopic results clearly indicate the success of our stepwise assembly strategy, in which the mono- and bimetallic species, with controllable metal nuclearity and constituent composition, can be precisely engineered.

## Determination of the metal-linker interaction

We first used X-ray photoelectron spectroscopy (Figures 2A, 2B, and S2; Table S2) and X-ray absorption near edge spectroscopy (Figure S3) to study the oxidation states of the samples. The oxidation states of +2 for Cu have been observed in all samples. This is consistent with our post-synthetic modulation approach, which does not involve any oxidative or reductive environment. Interestingly, noticeable peak shouldering is noted upon the introduction of external species due to the presence of $Cu^{2+}$ in multiple chemical environments. It is hence important to investigate if the variations in electronic structures originate from the formation of Cu–$N_{meIm}$ in

the proposed LMMEs. We have accordingly analyzed the ultraviolet-visible-near infrared (UV-vis-NIR) diffuse reflectance spectroscopy results in detail. As displayed in Figures 2C, 2D, S4, and S5, obvious variations are observed upon applications of the second metal species, which signify the formation of multinuclear meIm-mediated ensembles through coordination interactions. Extensive information can be extracted from the spectral data, including (1) broad and asymmetric transition centered at around 12,000 $cm^{-1}$ from the *d-d* transition in distorted octahedral aqua complexes of $Cu^{2+}$ (commonly seen in hydrated Cu-zeolites);[27] (2) a reversible trend in *d-d* absorption upon each meIm linker (i.e., $Cu_1$-meIm-Z and $Cu_2$-meIm-Z; hypsochromic shift) and the Cu step (i.e., $Cu_2$-Z and $Cu_3$-Z; bathochromic shift), which can be ascribed to the stronger Cu–meIm interaction than the original $Cu–OH_2$ interaction as meIm is a strong $\sigma$ donor and a weak $\pi$ acceptor ligand that enlarges the ligand field splitting $\Delta$; and (3) an apparent hypsochromic shift of absorption at above 45,000 $cm^{-1}$ (ligand-to-metal charge transfer) from Cu-Zn-Z to Cu-Co-Z, which suggests that the binding interactions are perturbed due to the difference in constituent elemental composition. In addition, the presence of meIm ligands and metal-ligand interactions have been verified by Fourier transform infrared spectroscopy (Figure S6), thermogravimetric analysis (Figure S7), and solid-state $^1H$ nuclear magnetic resonance spectroscopy (Figure S8).

## Elucidation of the atomic structures of LMMEs

The local structures of supported single atoms and nanoclusters can be discerned using extended X-ray absorption fine-structure spectroscopy (EXAFS). Accordingly, we first employed wavelet transformation (WT) to correlate the EXAFS data in both R- and k-spaces, as presented in Figures S9–S11. The WT-EXAFS data show only a major lobe centered at R = 1.5 Å (k = 7.0 $Å^{-1}$), which can be attributed to the back-scattering of N/O atoms around the Cu center. We do not observe any long-range Cu···Cu/M scattering path at higher R- (>2.5 Å) and k-spaces (>10 $Å^{-1}$), indicative of the absence of direct metal aggregation. As seen in the quantitative fitting of the EXAFS data (Tables S3 and S4), the average Cu–N/O bond lengths are calculated as ~1.9–2.0 Å. Meanwhile, the average Cu–N/O coordination number of $Cu_1$-Z was determined as 4 (indicative of a pseudo square planar coordination, from possible Jahn-Teller distortion), whereas those of $Cu_2$-Z, Cu-*M*-Z, and $Cu_3$-Z were determined as ~3 (trigonal planar $Cu^{2+}$ geometry,[28] potentially due to zeolite confinement).

As shown in the high-resolution synchrotron X-ray powder diffraction (SXRD) profiles in Figure S12, we observed only marginal shifts of the Bragg peaks (space group: *Pnma*), suggesting that the post-synthetic modulations did not significantly affect the crystalline framework of the host ZSM-5 zeolite. It is consistent with the morphology characterization results from scanning electron microscopy (SEM), transmission electron microscopy (TEM), and energy dispersive X-ray analysis (EDX) (Figure S13). The symmetric Bragg peaks indicate that the modified zeolites are highly homogeneous, which would enable the use of a crystallography-based strategy to elucidate the atomic and structural parameters of the extra-framework LMMEs. To ensure more reliable Rietveld refinements of the SXRD patterns, we have extracted key information from elemental and thermogravimetric analyses to construct rigid body Z matrices to better describe the LMMEs as the initial refinement input (Figure S14; Table S5), as done in our previous work.[29–33] Taking $Cu_2$-Z as an example, the Cu:meIm ratio is calculated as ~1:1. Therefore, we applied the initial rigid body Z matrix of $Cu_2$ as meIm–Cu–meIm–Cu, with the overall site-occupancy factors constrained.

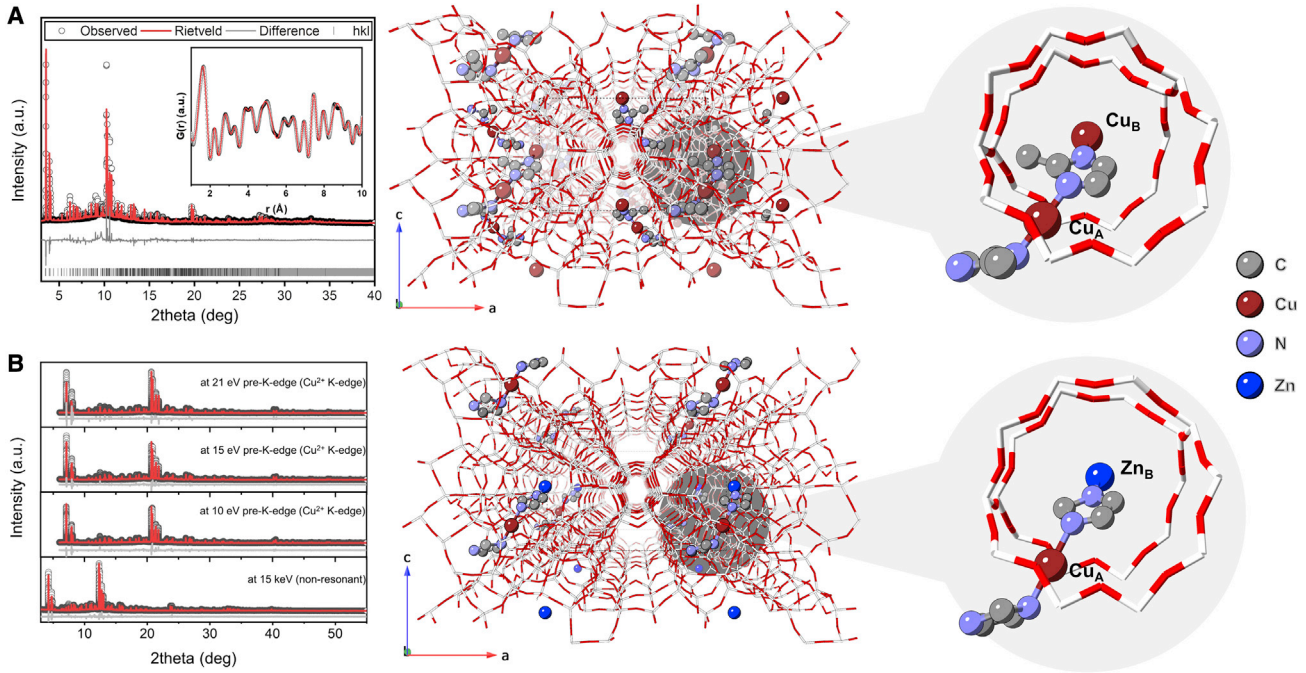


**Figure 3. Atomic and structural elucidation of monometallic and bimetallic LMMEs in ZSM-5**

(A) Rietveld refinement of SXRD data and the refined crystal structures of $Cu_2$-Z (inset: X-ray pair distribution function analysis profile).

(B) Resonant SXRD measurements of Cu-Zn-Z(Im).

Atoms are represented in balls and sticks; white and red sticks represent Al/Si and O, respectively. The refined crystal structures have been verified by DFT calculations as shown in Figures S24–S26.

The alteration of the scattering factors upon the incorporation of extra-framework metal sites and organic ligands is significant.[29,31] Hence, we have employed a comprehensive bulk approach to determine the crystal structures of the supported LMMEs and their atomic parameters by combining SXRD with whole-pattern modeling (Rietveld refinements), atom pair distribution function analysis, and density functional theory (DFT) calculations.

The crystallographic locations of the metal nuclei were first identified by the charge-flipping algorithm. For example, we observed two crystallographic Cu sites in $Cu_2$-Z that are located around 5.6 Å apart (Figure S15). This atomic separation implies a presence of a bridging mIm ligand between the two Cu nuclei, as it is consistent with the Cu···Cu interatomic distance in our proposed Cu–mIm–Cu structure. Accordingly, by further refinement, Figure 3A displays the optimized crystal structure of $Cu_2$-Z with the inclusion of mIm. As seen, the $Cu_A$ site is located at the intersection of the sinusoidal and straight channels, and the $Cu_B$ site is located at the opening of the straight channel. The closest interatomic distance between $Cu_A$ and framework O atoms is found at $Cu_A$···O18 of 3.40(1) Å, which agrees with our previous crystallographic findings where O18 is adjacent to the Al(T6) site.[29,31] The interatomic angle of $\angle Cu_A$-mIm-$Cu_B$ is determined as 134.1(3)°, which agrees with the typical values of related zeolitic imidazolate frameworks.[34] Meanwhile, Figures S16 and S17 show the optimized crystal structures of $Cu_x$-Z and $Cu_x$-mIm-Z; the corresponding atomic and structural parameters are summarized in Tables S6–S11. The consistency of the LMME structures upon sequential additions of $Cu^{2+}$ and mIm renders the stepwise modularity clearly.

Meanwhile, we have also studied the crystal structures of the bimetallic LMMEs (Cu-Co-Z, Cu-Ni-Z, and Cu-Zn-Z) using the same bulk approach (Figure S18; Tables S12–S15). Despite that neighboring metal species can hardly be differentiated by conventional X-ray techniques, the atom-by-atom analysis has initially identified the crystallographic locations of the metal sites. Thus, it is of utmost importance to determine the respective crystallographic locations of the constituent metal nuclei.

Accordingly, we used resonant SXRD, unique to synchrotron-based instruments, to determine the crystal structure of Cu-Zn-Z(Im) containing atoms with low electronic contrast. The resonant technique can differentiate elements with close atomic numbers, such as Co (Z = 27), Ni (Z = 28), Cu (Z = 29), and Zn (Z = 30), by exploiting the enhanced contrast between their anomalous scattering factors *f′* (real) and *f″* (imaginary). The diffraction measurements were collected at selected energies at the pre-K-edge of Cu (10, 15, and 21 eV) to maximize the contrast in *f′*. The high-resolution comparative SXRD measured at 15 keV is also required for an accurate determination of the zeolite framework (containing Si/Al and O atoms) as performed above. A combined Rietveld refinement approach has been meticulously performed to differentiate the respective locations of Cu and Zn sites (Figure 3B). A series of control procedures have been taken to test the sensitivity of the resonant SXRD refinement (Table S16). The X-ray absorption spectrum for Cu-K-edge determination and detailed Rietveld refinement profiles are presented in Figures S19–S23. The atomic and crystallographic parameters are summarized in Tables S17 and S18. Clearly, the $Cu_A$ site is located at the intersection of the straight and sinusoidal channels, and the $Zn_B$ site is located at the opening of the straight channel (Figures S24–S26). The crystal structures of $Cu_2$-Z and Cu-Zn-Z are comparable, which suggests the transferability of our stepwise assembly strategy.

## Theoretical calculations

To study the electronic structures of the LMMEs on zeolites with different metal constituents, we have presented the DFT-based theoretical investigations on $Cu_2$-Z and Cu-Co-Z as illustrations. Figures 4A and 4B shows significant variations in the electronic distributions in the three-dimensional contour plots. For $Cu_2$-Z, we notice that the electronic state is predominantly dominated by the $Cu_2$ LMME, while the zeolite support mainly contributes to the anti-bonding states, whereas for Cu-Co-Z, the electronic distribution is perturbed by the presence of the Co site compared with the $Cu_2$-Z analog, where both Cu and Co dominate the electronic states. The greater overlap of electronic distributions at the zeolite framework in Cu-Co-Z can facilitate electron transfer from the Cu-Co LMME to incoming substrates. Subsequently, we have studied their projected partial density of states, as displayed in Figures 4C and 4D. For $Cu_2$-Z, the sharp peak of Cu-3*d* orbitals occupies $E_v$ = -1.55 eV (Fermi level at 0 eV), where the adjacent meIm linker shows substantial overlap with Cu-3*d*. The zeolite framework O sites show a broad band that can facilitate electron transfer toward adsorbed substrates. In Cu-Co-Z, the Co site illustrates a more electroactive character than Cu, rendering a higher electron density near the Fermi level. The modulated electronic structure of Cu-Co-Z can facilitate electron transfer from the Cu-Co LMME through the Co site to adsorbed substrates. Notably, the presence of electronic communication between the metal nuclei can be seen. We also show that both electronic distributions and partial density of states can be modulated using a foreign metal species in bimetallic combinations, which would ultimately influence the catalytic properties.

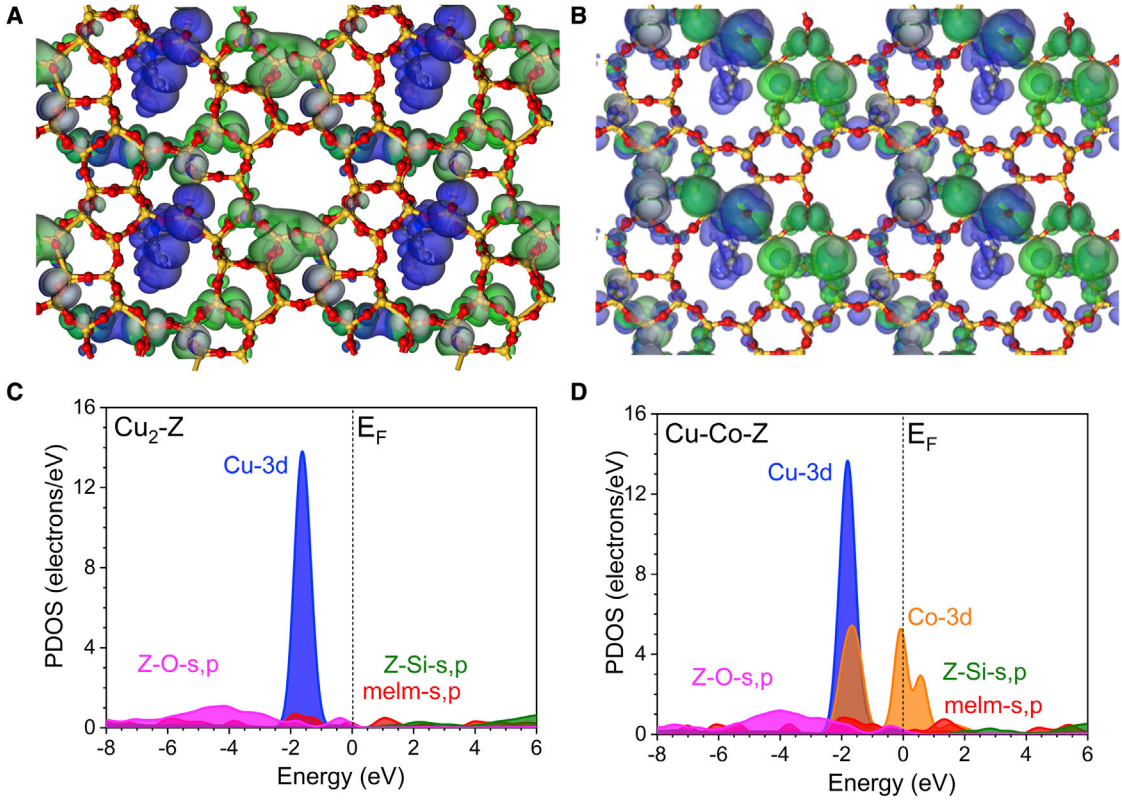


**Figure 4. DFT calculations of $Cu_2$-Z and Cu-Co-Z**

(A and B) The three-dimensional contour plot of the electronic distribution of (A) $Cu_2$-Z and (B) Cu-Co-Z, viewed along the crystallographic b axis.
(C and D) The partial density of states (PDOSs) of (C) $Cu_2$-Z and (D) Cu-Co-Z.
See also Figures S27 and S28.

## Catalytic click reaction as a chemical probe

Evidently, we have precisely engineered a series of supported Cu-based LMMEs (Cu-M [M = Co, Ni, Cu, and Zn] and $Cu_3$) in ZSM-5 zeolite via our stepwise assembly strategy. The atomic structures of the active sites are notably different compared with the mononuclear analog in two main aspects, namely, metal nuclearity and elemental constituent composition. Hereby, we have chosen the Huisgen azide-alkyne cycloaddition "click" reaction as a chemical probe to study these parameters because it requires a collaborative use of two active metal sites for substrate activation.[35,36] We first evaluated the nuclearity effect. As presented in Table 1, the catalytic conversions over $Cu_2$-Z (37.6%) and $Cu_3$-Z (37.2%) are more than an order of magnitude higher than the mononuclear $Cu_1$-Z analog (3.2%). The slight reactivity of $Cu_1$-Z can be attributed to the presence of proximate-but-dispersed Cu sites (as shown in our comparative study using ZSM-5 with a lower Al content in Table S19). The apparent difference in the catalytic reactivity between $Cu_1$-Z and $Cu_2$-Z suggests that the presence of neighboring Cu nuclei more preferentially favors the click-reaction mechanism, which requires the co-activation of the reaction substrates. Meanwhile, the marginal difference between $Cu_2$-Z and $Cu_3$-Z suggests that the third Cu site does not actively contribute to the click-reaction mechanism.

By varying the elemental constituent composition, we observed a declining trend of catalytic conversion across the samples, with Cu-Co-Z possessing the highest

**Table 1. Probing the effects on metal nuclearity and constituent composition of the LMME samples by the Huisgen azide-alkyne cycloaddition click reaction**

| Entry | Catalysts | Conversion (%)[a,b] |
|---|---|---|
| 1a | H-ZSM-5 | 0 |
| 1b | $Cu_1$-Z | 3.2 |
| 1c | $Cu_2$-Z | 37.6 |
| 1d | $Cu_3$-Z | 37.2 |
| 2a | Cu-Co-Z | 59.0 |
| 2b | Cu-Ni-Z | 40.9 |
| 2c | $Cu_2$-Z | 37.6 |
| 2d | Cu-Zn-Z | 24.3 |

[a]The conversion of phenylacetylene was determined using high-performance liquid chromatography (HPLC). See original data and detailed analysis of HPLC in Figures S30–S32. No metal leaching was detected. The chemostability and recyclability study is presented in Figures S33–S35 and Table S25, where the reactivity maintains for at least three catalytic cycles.
[b]The catalytic performance has been further optimized by applying different solvents and with the addition of N,N-diisopropylethylamine (DIEA; additive), as summarized in Table S26.

conversion at 59.0% and Cu-Zn-Z possessing the lowest conversion at 24.3%. Based on the DFT calculations, the overall adsorption of the reaction substrates on Cu-Co-Z (about -3.0 eV) is much more preferred than that on $Cu_2$-Z (about +0.2 eV; Figure S27). Figure S28 shows that the simulated activation energy for the click reaction over Cu-Co-Z is lower than that over $Cu_2$-Z (cf. 0.21 versus 0.33 eV). From our Rietveld-refined adsorbate structures (Figure S29; Tables S20–S24), phenylacetylene is adsorbed on the second metal site ($M_B$, from kinetic consideration) via $\eta^2$ side-on configuration. The elemental variation in the $M_B$ site can therefore influence the energy of the lowest unoccupied molecular orbital (LUMO) of adsorbed phenylacetylene (as a dipolarphile) based on the relative theoretical energy levels. Accordingly, $Co^{II}$ ($3d^7$) can lower the LUMO energy of the adsorbed phenylacetylene to a greater extent than $Zn^{II}$ ($3d^{10}$), which allows better energy matching with the highest occupied molecular orbital (HOMO) of the adsorbed benzyl azide (1,3-dipole). The difference in the catalytic reactivity suggests that the electronic structures of the LMMEs are clearly affected by different constituent metal species.

## DISCUSSION

In brief, we have demonstrated that atom-precise Cu-based mono- and bimetallic LMMEs can be engineered by utilizing the underlying principles of coordination chemistry and solid-state chemistry. Mid-to-late *3d* transition metal ions can be assembled by Lewis di-basic meIm linkers within the microporous cavity of ZSM-5 zeolites. The elemental composition and structural characteristics of the LMMEs have been elucidated by X-ray fluorescence spectroscopy and MALDI-TOF-TOF mass spectroscopy. The electronic and geometric properties have been revealed by a combination of crystallographic and diffraction techniques. Synergistic effects from the neighboring metal nuclei in the LMMEs are clearly pivotal to modulating the catalytic capability from the modification of the electronic and geometric properties. By exploiting the click reaction as a chemical probe, the adsorption strengths and activation energy can be optimized by altering the binuclear combination, such as $Cu_A$ and $Co_B$ in Cu-Co-Z from $Cu_A$ and $Cu_B$ in $Cu_2$-Z. However, the intrinsic limitations of solid-state materials, including experimental interference, material interactions, and less-defined active-site structure (as noted in our MS results, e.g., the residual presence of single Cu species in $Cu_2$-Z), etc., could make it much more challenging for materials characterization using conventional spectroscopic techniques.

This stepwise assembly strategy of multiple mid-to-late *3d* transition metal ions through di-basic linker molecules demonstrated in this work can be readily expanded to a much greater scope. We envisioned that multinuclear LMMEs comprised late *4d* transition metals and a combination of *3d* and *4d* late transition metals with variable multibasic linkers over different solid-state supports will also be engineered in the near future. While these mid-to-late transition metals at various oxidation states would exhibit rather unique redox and coordination characteristics, exploiting their oxidation states would create an effective catalytic landscape with favorable electronic and geometric properties for stabilizing the transition states and reaction intermediates of specific reactions, such as for cross-coupling reactions that could benefit from the presence of multiple neighboring metal nuclei. This work would offer a realizable leap toward next-generation heterogeneous catalysts at the molecular homogeneous dimension for the sustainable production of fine chemicals and would bring about a substantial impact on catalysis and materials communities.

## EXPERIMENTAL PROCEDURES

### Resource availability

#### *Lead contact*

Further information and requests for resources should be directed to and will be fulfilled by the lead contact, Tsz Woon Benedict Lo (twblo@polyu.edu.hk).

#### *Materials availability*

None of the unique materials generated in this study are readily available.

#### *Data and code availability*

All data needed to support the conclusions of this manuscript are included in the main text or the supplemental information.

## SUPPLEMENTAL INFORMATION

Supplemental information can be found online at https://doi.org/10.1016/j.xcrp.2022.100850.

## ACKNOWLEDGMENTS

We thank Diamond Light Source, SPring-8, and NSRRC for the provision of valuable synchrotron beamtime for SXRD and EXAFS measurements (CY26404 2020A1088 and 2020A0565). This work was supported by the Hong Kong Research Grants Council (15301521 and 15300819) and the National Natural Science Foundation of China (22172136) for financial support (T.W.B.L.). Finally, we thank UMF, UCEA, and UMF of PolyU for their support in materials characterization.

## AUTHOR CONTRIBUTIONS

T.W.B.L. conceived the project, directed the study, and wrote the manuscript. T.C. carried out the synthesis and characterizations and collaborated on writing the manuscript. Y.W. carried out catalytic measurements. Q.X. analyzed the EXAFS data. C.K.T.W. and P.K.S. carried out the mass spectroscopy measurements. T.-S.W. and Y.-L.S. collected the EXAFS data in NSRRC in Taiwan. K.T. collected the SXRD data in SPring-8. S.D. and C.C.T. collected the resonant-SXRD data in Diamond Light Source. Z.L. collected the XPS data. B.H. carried out theoretical calculations. S.C.E.T., K.F.Y., and K.-y.W. offered advice on catalysis and structure-reactivity correlations. All authors discussed the results and contributed to the production of the manuscript.

## DECLARATION OF INTERESTS

The authors declare no competing interests.

Received: October 19, 2021
Revised: February 26, 2022
Accepted: March 21, 2022
Published: April 8, 2022

## REFERENCES

1. Corma, A., Concepción, P., Boronat, M., Sabater, M.J., Navas, J., Yacaman, M.J., Larios, E., Posadas, A., López-Quintela, M.A., Buceta, D., et al. (2013). Exceptional oxidation activity with size-controlled supported gold clusters of low atomicity. Nat. Chem. *5*, 775–781.

2. Guan, J., Duan, Z., Zhang, F., Kelly, S.D., Si, R., Dupuis, M., Huang, Q., Chen, J.Q., Tang, C., and Li, C. (2018). Water oxidation on a mononuclear manganese heterogeneous catalyst. Nat. Catal. *1*, 870–877.

3. Ji, S., Jiang, B., Hao, H., Chen, Y., Dong, J., Mao, Y., Zhang, Z., Gao, R., Chen, W., Zhang, R., et al. (2021). Matching the kinetics of natural enzymes with a single-atom iron nanozyme. Nat. Catal. *4*, 407–417.

4. Coelho, P.S., Brustad, E.M., Kannan, A., and Arnold, F.H. (2013). Olefin cyclopropanation via carbene transfer catalyzed by engineered cytochrome P450 enzymes. Science *339*, 307–310.

5. Bols, M.L., Snyder, B.E.R., Rhoda, H.M., Cnudde, P., Fayad, G., Schoonheydt, R.A., Van Speybroeck, V., Solomon, E.I., and Sels, B.F. (2021). Coordination and activation of nitrous oxide by iron zeolites. Nat. Catal. *4*, 332–340.

6. Chen, X., Peng, M., Cai, X., Chen, Y., Jia, Z., Deng, Y., Mei, B., Jiang, Z., Xiao, D., Wen, X., et al. (2021). Regulating coordination number in atomically dispersed Pt species on defect-rich graphene for n-butane dehydrogenation reaction. Nat. Commun. *12*, 2664.

7. Yao, S., Zhang, X., Zhou, W., Gao, R., Xu, W., Ye, Y., Lin, L., Wen, X., Liu, P., Chen, B., et al. (2017). Atomic-layered Au clusters on α-MoC as catalysts for the low-temperature water-gas shift reaction. Science *357*, 389–393.

8. Vercammen, J., Bocus, M., Neale, S., Bugaev, A., Tomkins, P., Hajek, J., Van Minnebruggen, S., Soldatov, A., Krajnc, A., Mali, G., et al. (2020). Shape-selective C–H activation of aromatics to biarylic compounds using molecular palladium in zeolites. Nat. Catal. *3*, 1002–1009.

9. Leyva-Pérez, A. (2017). Sub-nanometre metal clusters for catalytic carbon-carbon and carbon-heteroatom cross-coupling reactions. Dalton Trans. *46*, 15987–15990.

10. Khoshsefat, M., Ma, Y., and Sun, W.H. (2021). Multinuclear late transition metal catalysts for olefin polymerization. Coord. Chem. Rev. *434*, 213788.

11. Hanhan, M.E., Cetinkaya, C., and Shaver, M.P. (2013). Effective binuclear Pd(II) complexes for Suzuki reactions in water. Appl. Organomet. Chem. *27*, 570–577.

12. Xia, B.H., Zhang, H.X., Che, C.M., Leung, K.H., Phillips, D.L., Zhu, N., and Zhou, Z.Y. (2003). Metal-metal interactions in heterobimetallic d8-d10 complexes. Structures and spectroscopic investigation of [M′M″(μ-dcpm) 2(CN)2]+ (M′ = Pt, Pd; M″ = Cu, Ag, Au) and related complexes by UV-vis absorption and resonance Raman spectroscopy and ab initio calculations. J. Am. Chem. Soc. *125*, 10362–10374.

13. Zhao, S., Tan, C., He, C.T., An, P., Xie, F., Jiang, S., Zhu, Y., Wu, K.H., Zhang, B., Li, H., et al. (2020). Structural transformation of highly active metal–organic framework electrocatalysts during the oxygen evolution reaction. Nat. Energy *5*, 881–890.

14. Jin, R., Peng, M., Li, A., Deng, Y., Jia, Z., Huang, F., Ling, Y., Yang, F., Fu, H., Xie, J., et al. (2019). Low temperature oxidation of ethane to oxygenates by oxygen over iridium-cluster catalysts. J. Am. Chem. Soc. *141*, 18921–18925.

15. McKenzie, C.J., and Robson, R. (1988). High turnover catalysis at bimetallic sites of the hydration of nitriles to carboxamides co-catalysed by acid. Highly specific hydration of acrylonitrile to acrylamide. J. Chem. Soc. Chem. Commun. *112*, 112–114.

16. Nagashima, H., Sue, T., Oda, T., Kanemitsu, A., Matsumoto, T., Motoyama, Y., and Sunada, Y. (2006). Dynamic titanium phosphinoamides as unique bidentate phosphorus ligands for platinum. Organometallics *25*, 1987–1994.

17. Feng, G., Zhang, M., Shao, D., Wang, X., Wang, S., Maron, L., and Zhu, C. (2019). Transition-metal-bridged bimetallic clusters with multiple uranium–metal bonds. Nat. Chem. *11*, 248–253.

18. Eisenhart, R.J., Clouston, L.J., and Lu, C.C. (2015). Configuring bonds between first-row transition metals. Acc. Chem. Res. *48*, 2885–2894.

19. Török, I., Surdy, P., Rockenbauer, A., Korecz, L., Jr., Anthony, A., Koolhaas, G.J., and Gajda, T. (1998). Nickel(II)-, copper(II)- and zinc(II)-complexes of some substituted imidazole ligands. J. Inorg. Biochem. *71*, 7–14.

20. Coutiño-Gonzalez, E., Baekelant, W., Steele, J.A., Kim, C.W., Roeffaers, M.B.J., and Hofkens, J. (2017). Silver clusters in zeolites: from self-assembly to ground-breaking luminescent properties. Acc. Chem. Res. *50*, 2353–2361.

21. Chen, T., Xue, Q., Leung, K.C., and Lo, B.T.W. (2020). Recent advances of precise Cu nanoclusters in microporous materials. Chem. Asian J. *15*, 1819–1828.

22. Peng, M., Dong, C., Gao, R., Xiao, D., Liu, H., and Ma, D. (2021). Fully exposed cluster catalyst (FECC): toward rich surface sites and full atom utilization efficiency. ACS Cent. Sci. *7*, 262–273.

23. Goswami, A., and Schmittel, M. (2020). Double rotors with fluxional axles: domino rotation and azide–alkyne huisgen cycloaddition catalysis. Angew. Chem. Int. Ed. *59*, 12362–12366.

24. Sroka-Bartnlcka, A., Ciesielski, W., Libiszowski, J., Duda, A., Sochaeki, M., and Potrzebowski, M.J. (2010). Complementarity of solvent-free MALDI TOF and solid-state NMR spectroscopy in spectral analysis of polylactides. Anal. Chem. *82*, 323–328.

25. Dass, A., Stevenson, A., Dubay, G.R., Tracy, J.B., and Murray, R.W. (2008). Nanoparticle MALDI-TOF mass spectrometry without fragmentation: Au 25 (SCH 2 CH 2 Ph) 18 and mixed monolayer Au 25 (SCH 2 CH 2 Ph) 18− x (L) x. J. Am. Chem. Soc. *130*, 5940–5946.

26. Zavras, A., Khairallah, G.N., Connell, T.U., White, J.M., Edwards, A.J., Donnelly, P.S., and O'Hair, R.A.J. (2013). Synthesis, structure and gas-phase reactivity of a silver hydride complex [Ag 3 {(PPh 2 ) 2 CH 2 } 3 (μ 3 -H)(μ 3 -Cl)]BF 4. Angew. Chem. Int. Ed. *52*, 8391–8394.

27. Giordanino, F., Vennestrøm, P.N.R., Lundegaard, L.F., Stappen, F.N., Mossin, S., Beato, P., Bordiga, S., and Lamberti, C. (2013). Characterization of Cu-exchanged SSZ-13: a comparative FTIR, UV-Vis, and EPR study with Cu-ZSM-5 and Cu-β with similar Si/Al and Cu/Al ratios. Dalton Trans. *42*, 12741–12761.

28. Godiksen, A., Vennestrøm, P.N.R., Rasmussen, S.B., and Mossin, S. (2017). Identification and quantification of copper sites in zeolites by electron paramagnetic resonance spectroscopy. Top. Catal. *60*, 13–29.

29. Chen, T., Huang, B., Day, S., Tang, C.C., Tsang, S.C.E., Wong, K.Y., and Lo, T.W.B. (2020). Differential adsorption of l- and d-lysine on achiral MFI zeolites as determined by synchrotron X-ray powder diffraction and thermogravimetric analysis. Angew. Chem. Int. Ed. *59*, 1093–1097.

30. Lo, B.T.W., Ye, L., and Tsang, S.C.E. (2018). The contribution of synchrotron X-ray powder diffraction to modern zeolite applications: a mini-review and prospects. Chem *4*, 1–31.

31. Lo, B.T.W., Ye, L., Qu, J., Sun, J., Zheng, J., Kong, D., Murray, C.A., Tang, C.C., and Tsang, S.C.E. (2016). Elucidation of adsorbate structures and interactions on brønsted acid sites in H-ZSM-5 by synchrotron X-ray powder diffraction. Angew. Chem. Int. Ed. *55*, 5981–5984.

32. Ye, L., Song, Q., Lo, B.T.W., Zheng, J., Kong, D., Murray, C.A., Tang, C.C., and Tsang, S.C.E. (2017). Decarboxylation of lactones over Zn/ZSM-5: elucidation of the structure of the active site and molecular interactions. Angew. Chem. Int. Ed. *56*, 10711–10716.

33. Lo, B.T.W., Lin, W.C., Li, M.M.J., Day, S., Tang, C., and Tsang, S.C.E. (2020). Evaluation of Brønsted and Lewis acid sites in H-ZSM-5 and H-USY with or without metal modification using probe molecule-synchrotron X-ray powder diffraction. Appl. Catal. Gen. *596*, 117528.

34. Zheng, B., Sant, M., Demontis, P., and Suffritti, G.B. (2012). Force field for molecular dynamics computations in flexible ZIF-8 framework. J. Phys. Chem. C *116*, 933–938.

35. García-García, P., Müller, M., and Corma, A. (2014). MOF catalysis in relation to their homogeneous counterparts and conventional solid catalysts. Chem. Sci. *5*, 2979–3007.

36. Worrell, B.T., Malik, J.A., and Fokin, V.V. (2013). Direct evidence of a dinuclear copper intermediate in Cu(I)-catalyzed azide-alkyne cycloadditions. Science *340*, 457–460.